Pis'ma v ZhETF, vol. 81, iss. 6, pp. 351 – 355

Spin fluctuations in the stacked-triangular antiferromagnet $YMnO_3$

B. Roessli[+], *S. N. Gvasaliya*[*+], *E. Pomjakushina*[+□], *K. Conder*[□]

[+]*Laboratory for Neutron Scattering ETHZ & Paul Scherrer Institute, CH-5232 Villigen PSI, Switzerland*

[*]*Ioffe Physical Technical Institute, 194021 St. Petersburg, Russia*

[□]*Laboratory for Development and Methods, Paul Scherrer Institut, CH-5232 Villigen PSI, Switzerland*

Submitted 24 February 2005

The spectrum of spin fluctuations in the stacked-triangular antiferromagnet $YMnO_3$ was studied above the Néel temperature using both unpolarized and polarized inelastic neutron scattering. We find an in-plane and an out-of-plane excitation. The in-plane mode has two components just above T_N, a resolution-limited central peak and a Debye-like contribution. The quasi-elastic fluctuations have a line-width that increases with q like Dq^z and the dynamical exponent $z = 2.3$. The out-of-plane fluctuations have a gap at the magnetic zone center and do not show any appreciable q-dependence at small wave-vectors.

PACS: 75.40.–s, 78.70.Nx

1. Introduction. $YMnO_3$ belongs to the family of $RMnO_3$ (R=Rare-earth) manganite ferroelectric compounds that crystallize in the hexagonal space-group $P6_3cm$ below the paraelectric-ferroelectric phase transition ($\sim$ 900 K). In $YMnO_3$ the Mn^{3+}-ions form triangular layers well separated from each other by Y-layers. Because in the ferroelectric phase the lattice is distorted, the Mn-ions are slightly trimerized. The large separation between adjacent layers suggests that $YMnO_3$ forms a good candidate of a geometrically frustrated 2-Dimensional (2D) antiferromagnet.

The magnetic structure of hexagonal $YMnO_3$ was first investigated by Bertaut and Mercier [1] and re-investigated later in more details by Mu noz et al. [2]. Below T_N $\sim$70 K, the $S = 2$ magnetic moment of Mn-ions are arranged in a 120° magnetic structure with the triangular layers at z=0 and z=1/2 being antiferromagnetically coupled. At saturation the magnetic moment is μ=2.9 μ_B, i.e. significantly reduced from the expected 4μ_B of Mn^{3+} spins, which was taken as evidence that even in the ordered phase strong spin fluctuations are present as a consequence of geometrical frustration [3]. Analysis of the spin-wave spectrum have confirmed the 2D character of the magnetic exchange interactions in $YMnO_3$ [4] with the ratio of intra- to inter-plane exchange interactions being of the order $\sim 2\cdot 10^2$. Whereas well-defined excitations are observed below the ordering temperature, a broad inelastic signal as well as short-range correlations between the Mn magnetic moments within the triangular layers persist well above T_N [3].

In this work we investigate the q and temperature dependence of the spin excitations in $YMnO_3$ close to the Néel temperature. We were motivated by the fact that the nature of the phase transition of frustrated magnets is still not completely understood and that the critical properties of stacked triangular antiferromagnets have received special attention since Kawamura [5] proposed that the critical exponents in these systems form a new universality class. Experimental confirmation of the new class of (chiral) exponents was found in $CsMnBr_3$ by unpolarized [6] and polarized neutron scattering [7] measurements as well as in Ho [8]. Second an anomaly in the dielectric constant ϵ with the electric field applied in the ab plane was found in $YMnO_3$ [9] at T_N. The nature of the coupling between electric and magnetic properties in hexagonal manganites is a subject of intense debate [10]. Clearly it is required to characterise the behavior of the magnetic fluctuations in the vicinity of T_N to understand the possible relationship with the magneto-dielectric effect in $YMnO_3$ [11].

2. Experimental. Polycrystalline $YMnO_3$ was prepared by a solid state reaction. Starting materials of Y_2O_3 and MnO_2 with 99.99% purity were mixed and grounded and then treated at temperature 1000–1200 C in air during at least 70 h with several intermediate grindings. The phase purity of the compound was checked with conventional x-ray diffractometer (SIEMENS D500). The powder was hydrostatically pressed in the form of rods (8 mm in diameter and $\sim$ 60 mm in length). The rods were subsequently sintered at 1300 C during 30 h. The crystal growth was carried out using an Optical Floating Zone Furnace (FZ-T-10000-H-IV-VP-PC, Crystal System Corp., Japan) with four 1000 W halogen lamps as a heat source. The growth rate was 1.5 mm/h and both rods (feeding and seeding rod) were rotated at about 20 rpm in opposite directions

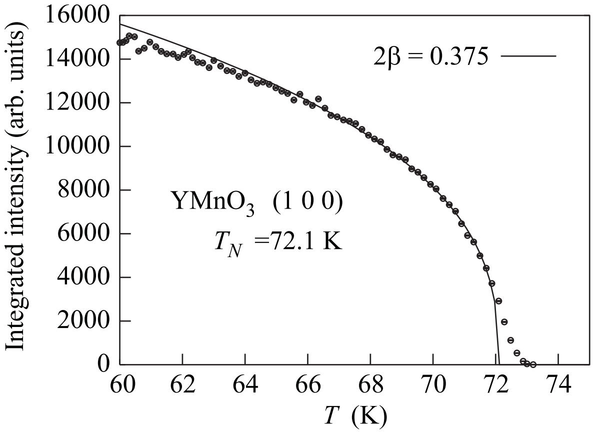

Fig.1. Temperature dependence of the intensity of (1 0 0) magnetic Bragg peak. The line is a fit to the data with a power law

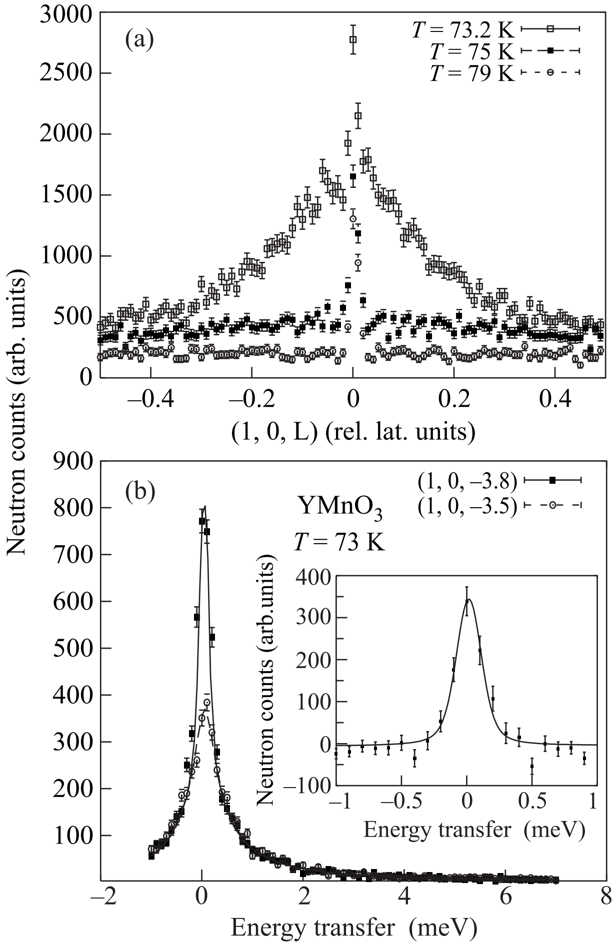

Fig.2. (a) Elastic scans along $(1,0,l)$ that show the increase of diffuse magnetic scattering in $YMnO_3$ when the temperature approaches T_N. (b) Inelastic scan that shows the presence of the central peak in $YMnO_3$. The insert shows the difference between scans measured at $(1,0,-3.8)$ and $(1,0,-3.5)$ that emphasizes the resolution-limited component

to ensure liquid homogeneity. A mixture of argon with 2% of oxygen at 5.5 bar was applied during growing. The crystal has the shape of a rod with 6 mm diameter and 2 cm height and a mosaic spread better than 1°.

The measurements were performed at triple-axis TASP located on the cold source of the neutron spallation source SINQ. The sample was mounted inside an He-flow cryostat with the crystallographic axis a^* and c^* in the scattering plane. The spectrometer was operated with the energy of the scattered neutrons kept fixed at k_f=1.47 Å^{-1} for measurements with unpolarized neutrons. 80′ Soller collimators were installed in the incident beam and before the analyzer and the detector. With that configuration the energy resolution at zero energy transfer is 180 μeV. To reduce both the background and contamination by higher wavelength neutrons a cold Be-filter was installed in the scattered beam. The inelastic polarized neutron measurements were performed at k_f=1.51 Å^{-1} along $(1 \pm q, 0, 0.1)$ and at different temperatures above T_N. To perform longitudinal-polarization analysis remanent supermirror benders [12] were inserted after the monochromator and before the analyser. The orientation of the polarization was chosen perpendicular to the scattering plane. Because magnetic fluctuations with polarization factor parallel to the neutron spin occur in the non-spin flip channel, the non-spin-flip data (NSF) contains the in-plane-fluctuations and in the spin-flip channel (SF) only out-of-plane fluctuations are present, as will be shown below.

3. Results and Discussion. Fig.1 shows the intensity of the (1 0 0) magnetic Bragg reflection as a function of temperature which mirrors the square of the staggered magnetization. The transition temperature, as determined by taking the derivative of the magnetization curve [13], is T_N=72.1±0.05 K. The intensity of the Bragg peak follows a power law $I \propto |(T/T_N - 1)|^{2\beta}$ with β=0.187(2). This value is lower than reported for the case of typical stacked-triangular antiferromagnet $RbNiCl_3$ (β=0.28), $CsNiCl_3$ (β=0.28), $CsMnBr_3$ (0.21< β <0.25) and close to the critical exponent obtained in VCl_2 (β=0.20) [5, 14]. Typical 2D XY antiferromagnets ($BaNi_2(PO_4)_2$), or ferromagnets (Rb_2CrCl_4, K_2CuF_4) have a magnetization exponent that corresponds to the expected theoretical value β=0.23 [15]. We note that β=0.19 in the 3D triangular Ising antiferromagnet [16]

Fig.2a shows elastic scans along the [1 0 l] direction as a function of temperature. Close to the Néel temperature, correlations between adjacent hexagonal planes give rise to broad magnetic scattering along c^* that eventually appears to condense into the magnetic Bragg peak

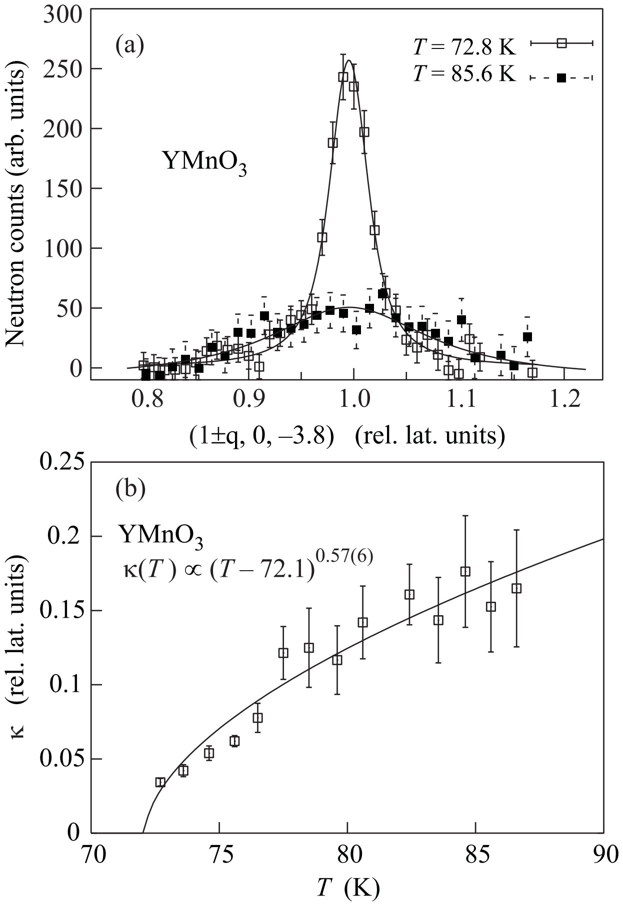

Fig.3. (a) Neutron diffuse intensity in $YMnO_3$. The background was measured at $T = 300$ K and has been subtracted. (b) Temperature dependence of the inverse of the correlation length. The line is a fit to the data with a power law

at T_N. From Fig.2b we see that this diffuse scattering is static on the time-scale of our experiment and corresponds to slow fluctuations of in-plane character, as will be shown below. With increasing temperature these correlations disappear and only scattering across the $[1\,0\,l]$-direction show a peak in the neutron cross-section. Hence, well above T_N correlations persist only between Mn moments located in the hexagonal plane, as shown in Fig.3. Here we describe the line-shape of the diffuse intensity by a Lorentzian profile convoluted with the resolution function of the spectrometer:

$$\chi_c(\mathbf{Q}) = \frac{\chi_0}{\pi} \frac{\kappa_\parallel^2}{(\mathbf{q}_\parallel - \mathbf{Q_0})^2 + \kappa_\parallel^2} \frac{\kappa_\perp^2}{(\mathbf{q}_\perp - \mathbf{Q_0})^2 + \kappa_\perp^2} \delta(\omega), \tag{1}$$

where $\mathbf{Q}_0$ is the position of the magnetic rod in reciprocal space; $\parallel$ and $\perp$ denotes direction along and perpendicular to the magnetic rod; $\kappa_\parallel$ the inverse of the correlation length ξ between Mn-spins in the hexagonal plane. Close to the Néel temperature, the temperature dependence of ξ behaves like $\xi(T) = 0.038(\pm 0.005) \times \times (T - T_N)^\nu$ with $\nu = 0.57(\pm 0.06)$ as shown in Fig.3b.

We turn now to the behavior of the paramagnetic fluctuations in $YMnO_3$. Figure 4 shows typical energy scans performed at $\mathbf{Q} = (1 - q, 0, -3.8)$ and $T = 73.6$ K. The inelastic cross-section for an unpolarized neutron beam is given by

$$\frac{d^2\sigma}{d\Omega d\omega} \propto \sum_{\alpha\beta} (\delta_{\alpha\beta} - \hat{Q}_\alpha \hat{Q}_\beta) S^{\alpha\beta}(\mathbf{Q}, \omega), \tag{2}$$

where $\delta_{\alpha\beta}$ is the Kronecker symbol, α, β are the Cartesian coordinates x, y, z, $(\mathbf{Q}, \omega)$ denote the momentum and energy transfers from neutron to sample and $\hat{Q} = = \mathbf{Q}/|\mathbf{Q}|$. The first term in Eq. (2) is a selection rule that implies that only spin components perpendicular to the scattering vector contribute to the neutron scattering cross-section. Hence, for scattering vectors with large l-components like $\mathbf{Q} = (1 \pm q, 0, -3.8)$, the inelastic spectrum contains essentially paramagnetic fluctuations with in-plane character ($\|$). In addition, close to the Néel temperature, inelastic scans through the magnetic rod show the resolution-limited central peak described by Eq. (1) as shown in Fig.2. Thus, to analyze the data shown in Fig.4, we modeled the inelastic intensity $I(\mathbf{Q}, \omega)$ in the following way

$$I(\mathbf{Q}, \omega) = (S^{\|}_{\mathrm{para}}(\mathbf{Q}, \omega) + \\ + S_{\mathrm{inc}}(\omega) + S\chi_c(\mathbf{Q})) \otimes R(\mathbf{Q}, \omega) + Bck, \tag{3}$$

where $S_{\mathrm{inc}} = A\delta(\omega)$ refers to the resolution-limited incoherent scattering that was measured at high temperature and S is a scale factor. The neutron scattering function $S^{\|}_{\mathrm{para}}(\mathbf{Q}, \omega)$, which is related to the imaginary part of the dynamical susceptibility through $\pi(g\mu_B)^2 S^{\|}_{\mathrm{para}}(\mathbf{Q}, \omega) = F^2(Q)(1 - \exp(-\hbar\omega/k_B T))^{-1} \Im\chi^{\|}(\mathbf{Q}, \omega)$, describes the line-shape of the paramagnetic scattering as a function of momentum ($\mathbf{Q}$) and energy ($\hbar\omega$) transfer, respectively. $F(Q)$ is the magnetic form factor of Mn. In Eq. (3), the symbol $\otimes$ stands for the convolution with the spectrometer resolution function $R(\mathbf{Q}, \omega)$ [17] and Bck denotes the background level. We find that a Debye-like quasi-elastic line-shape for the imaginary part of the dynamical susceptibility

$$\Im\chi^{\|}(\mathbf{Q_0} + \mathbf{q}, \omega) = \omega\chi(\mathbf{Q_0} + \mathbf{q}) \frac{\Gamma(\mathbf{q})}{\omega^2 + \Gamma(\mathbf{q})^2} \tag{4}$$

reproduces the data adequately. $\chi(\mathbf{q})$ is the static susceptibility as in Eq. (1) taken relative to the antiferromagnetic zone center ($\mathbf{Q_0}=(1,0,0)$) and $\Gamma(\mathbf{q})$ is the

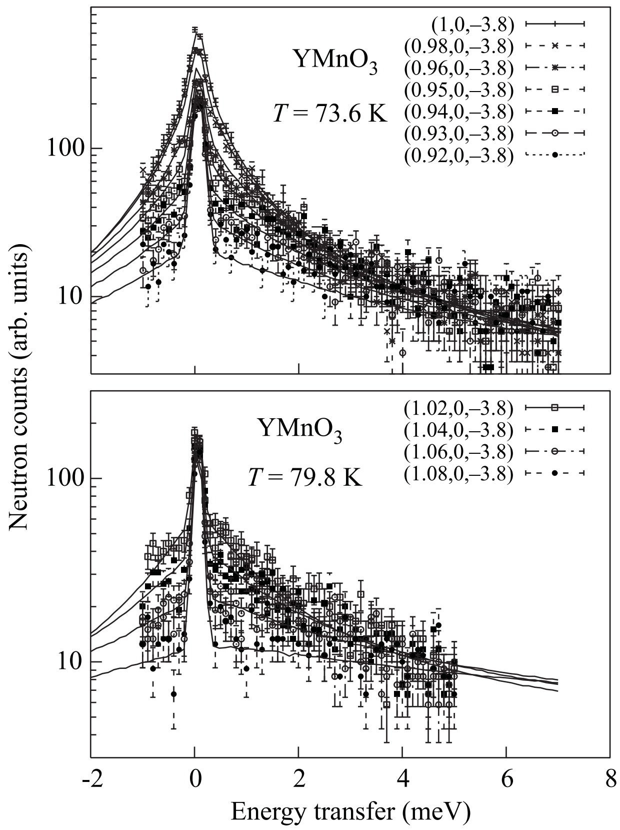

Fig.4. Constant q-scans in $YMnO_3$ at $T = 73.6$ K and 79.8 K that show the in-plane fluctuations, as explained in the text. The lines are the result of fit to the data using Eq. (3)

damping of the paramagnetic fluctuations. Figure 4 shows the results of fits to the data at $T = 73.6$ K from which we extract that the damping of the in-plane fluctuations $\Gamma(\mathbf{q})$ evolves like $\Gamma(0,T)+(1450\pm90)q^z$ (meV) with $\Gamma(0,73.6\text{ K})=0.23\pm0.07$ (meV), and $z=2.26\pm0.07$. In contrast with data taken around ($1\pm q$,0,3.8) the inelastic spectra around ($1\pm q$,0,0.1) cannot be fitted with Eq. (4). This is an indication that the spectrum of paramagnetic fluctuations in $YMnO_3$ consists of 2 modes, an in-plane ($\|$) as well as an out-of-plane component ($\perp$). To separate the $\|$- from the $\perp$-fluctuations, it is necessary to use polarization analysis. A typical inelastic spectrum measured with polarization analysis is shown in Fig.5 that reveals an out-of-plane excitation in the spin-flip channel. In contrast with the $\|$-fluctuations, the $\perp$-component is inelastic and is best described by a damped-harmonic oscillator function

$$S^{\perp}_{DHO} \propto \frac{\omega}{1-\exp(-\omega/T)}\frac{\gamma_q}{(\omega^2-\Omega_q^2)^2+\omega^2\gamma_q^2}, \qquad (5)$$

where Ω_q is the renormalized frequency and γ_q the damping of the excitation. Within the precision of the measurements we find that $\Omega_q=3.9\pm0.3$ (meV) and

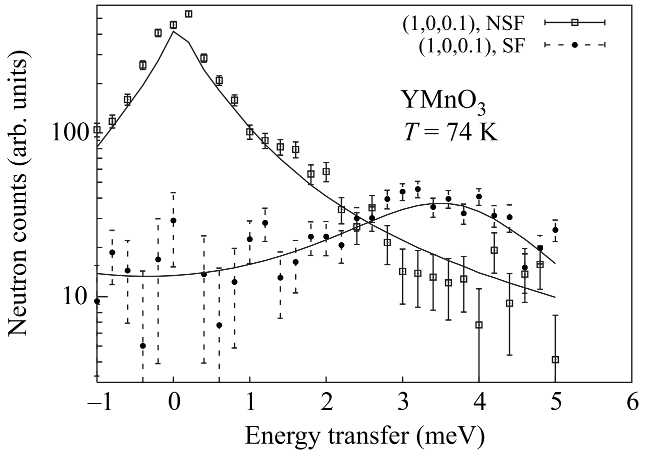

Fig.5. Constant q-scans in $YMnO_3$ at $T = 73.6$ K that show the in-plane fluctuations in the non-spin flip (NSF) and the out-of-plane component in the spin-flip channel (SF), respectively. The lines are the result of fit to the data as described in the text

$\gamma_q=2\pm0.5$ (meV) in the range of momentum values reached in the present experiment ($q\leq0.1$).

Parameter values for the damping ($\Gamma(\mathbf{q})=\gamma q^z$ (meV)) and the critical exponent (z) of the $\|$-fluctuations in $YMnO_3$

	T (K)	γ	$\Delta\gamma$	z	Δz
unpol.	73.6	1450	90	2.26	0.07
	79.8	1283	272	2.29	0.16
pol.	74	1306	277	2.53	0.25
	78	1028	313	2.40	0.4

The analysis of the data in the non-spin-flip channel yields the same q-dependence for the $\|$-fluctuations than was obtained with the unpolarized set-up. The results are summarized in the Table. The mean value for the dynamical exponent of the $\|$-fluctuations in $YMnO_3$ yields $z\sim2.3$ and does not agree with the theoretical dynamical exponent z=1 for the classical 2D triangular antiferromagnet [18]. Also the value obtained in $YMnO_3$ is quite different from the dynamical exponents z=1.5 expected for the 3D Heisenberg antiferromagnet and measured e.g. in $RbMnF_3$ [19] and $CsMnBr_3$ [20]. Finally we show the temperature dependence of $\Gamma(0,T)$ in Fig.6 that increases almost linearly above T_N, $\Gamma(0,T)=0.4+0.07\cdot(T-T_N)^{1.1\pm0.2}$.

4. Conclusion. To conclude, using both unpolarized and polarized inelastic neutron scattering, we showed that there are two magnetic excitations in the paramagnetic regime of $YMnO_3$ that have in-plane and an out-of-plane polarization, respectively. The in-plane mode has a resolution-limited central peak and a quasi-

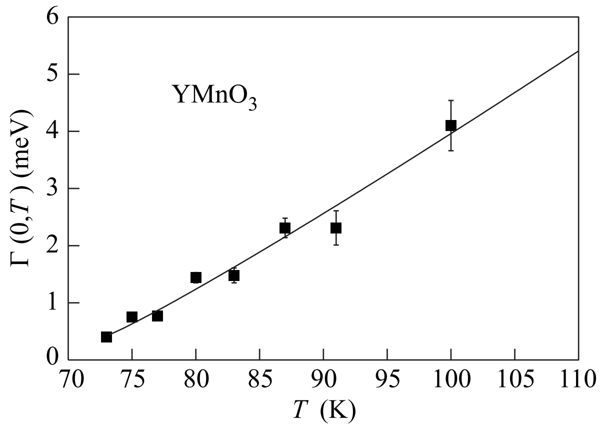

Fig.6. Temperature dependence of the damping of the paramagnetic fluctuations with in-plane polarization as measured with polarized neutrons. The line is a fit to the data as explained in the text

elastic component with a line-width that increases as a function of momentum transfer q like $\propto q^z$ with the dynamical exponent z=2.3. The presence of two time-scales in the spectrum of in-plane flucutations might be the signature for the coexistence of 2D and 3D fluctuations in the vicinity of T_N [21]. The out-of-plane fluctuations are inelastic at the magnetic zone center and do not show any q-dependence for small wave-vectors.

This work has been performed at the Neutron Spallation Source SINQ, Paul Scherrer Institut, Switzerland and was partly supported by NCCR MaNEP project.

1. B. Bertaut and M. Mercier, Phys. Lett. **5**, 27 (1963).
2. A. Munoz, J.A. Alonso, M.J. Martínez-Lope et al., Phys. Rev. **B62**, 9498 (2000).
3. Junghwan Park, J.-G. Park, Gun Sang Jeon et al., Phys. Rev. **B68**, 104426 (2003).
4. T. J. Sato, S.H. Lee, T. Katsufuji et al., Phys. Rev. **B68**, 014432 (2003).
5. For a recent Review see H. Kawamura, J. Phys.: Condens. Matter **10**, 4707 (1998).
6. T. E. Mason, B. D. Gaulin, and M. F. Collins, Phys. Rev. **B39**, 586 (1989).
7. V.P. Plakhty et al., Europhys. Lett. **48**, 215 (1999); V.P. Plakhty *et al.*, Phys. Rev. Lett. **85**, 3942 (2000).
8. V.P. Plakhty, W. Schweika, Th. Brückel et al., Phys. Rev. **B64**, 100402(R), 2001.
9. Z. J. Huang et al., Phys. Rev. **B56**, 2623 (1997); T. Katsufuji et al. Phys. Rev. **B64**, 104419 (2001).
10. T. Kimura et al. Nature **426**, 55 (2003); D. V. Efremov et al., Nature Materials **3**, 853 (2004); B. Lorenz et al., Phys. Rev. Lett. **92**, 087204 (2004).
11. G. Laws, A. P. Ramirez, C. M. Varma et al. Phys. Rev. Lett. **91**, 257208 (2003).
12. F. Semadeni, B. Roessli, and P. Böni, Physica **B297**, 152 (2001).
13. A. D. Bruce, J. Phys. **C14**, 193 (1982).
14. M. F. Collins and O. A. Petranko, Can. J. Phys. **75**, 605 (1997).
15. S. T. Bramwell and P. C. W. Holdsworth, J. Phys.: Condens. Matter **5**, L53 (1993).
16. O. Heinonen and R. G. Petschek, Phys. Rev **B40**, 9052 (1989).
17. M. Popovichi, Acta Cryst. **A31**, 507 (1975).
18. Kwangsik Nho and D.P. Landau, Phys. Rev. **B66**, 174403 (2002).
19. R. Coldea, R. A. Cowley, T. G. Perring et al., Phys. Rev. **B57**, 5281 (1998).
20. T. E. Mason, Y. S. Yang, M. F. Collins et al., J.M.M.M. **104-107**, 197 (1992).
21. L. P. Regnault, C. Lartigue, J. F. Legrand et al. Physica **B156-157**, 298 (1989); A. R. Völkel, A. R. Bishop, F. G. Mertens et al. J. Phys.: Condens. Matter **4**, 9411 (1992).